PAPER

Check for updates

Straightforward electrochemical synthesis of a Co₃O₄ nanopetal/ZnO nanoplate p−n junction for photoelectrochemical water splitting

Khanh Quang Nguyen,[abc] Hoang Thai Nguyen,[bc] Thach Khac Bui,[a] Tien-Thanh Nguyen[d] and Viet Van Pham [ID] *[a]

Hydrogen production through photoelectrochemical (PEC) reactions is an innovative and promising approach to producing clean energy. The PEC working electrode of a Co₃O₄/ZnO-based p−n heterojunction was prepared by a straightforward electrochemical deposition with different deposition times onto an FTO (Fluorine-doped Tin Oxide) glass substrate. The successful synthesis of the materials was confirmed through analysis using XRD, FTIR, SEM-EDX, DRS, and PL techniques. Mott−Schottky plots and some characterization studies also checked the determination of the formation of the p−n junction. Co₃O₄/ZnO/FTO with a Co₃O₄ deposition time of 2 minutes exhibited the lowest onset potential of 0.82 V and the lowest overpotential of 470 mV at a current density of 10 mA cm^{-2}. Furthermore, the photo-conversion efficiency of the Co₃O₄/ZnO/FTO sample showed 1.4 times higher current density than the ZnO/FTO sample. A mechanism is also proposed to enhance the Co₃O₄/ZnO/FTO electrode photo-electrocatalytic activity involved in the water-splitting reaction. The Co₃O₄/ZnO/FTO electrode shows significant potential as a promising PEC electrode to produce hydrogen.

1. Introduction

Solar-driven water splitting using semiconductors, including photochemical and photoelectrochemical (PEC) approaches, is receiving significant attention in energy research as a promising solution for clean and renewable energy generation.[1,2] The research of particulate semiconductor materials for photo-catalytic water splitting has emerged as a straightforward and environmentally friendly method for the efficient production of hydrogen.[3] Efficient photochemical water splitting requires photocatalysts with a band gap higher than the thermodynamic energy requirement of 1.23 eV. Also, the conduction band (CB) needs to be positioned negatively relative to the water reduction potential (H$^+$/H₂; 0 V *vs.* NHE), while the valence band (VB) should be active in a more positive potential region compared to the water oxidation potential (O₂/H₂O; 1.23 V *vs.* NHE).[4–6] Also, the efficiency of photocatalytic water splitting, which converts solar energy into hydrogen, has remained relatively low. For instance, Zhou *et al.*[7] conducted a study using InGaN/GaN

nanowire semiconductors, which achieved one of the highest solar-to-hydrogen efficiencies of 9.2% when using pure water under a xenon lamp with an AM1.5G filter. Integrating elec-trochemical processes with solar energy in PEC water splitting holds great potential as a highly effective approach for enhancing hydrogen production efficiency.[8] The primary components of PEC cells consist of a photoactive semi-conductor electrode submerged in an appropriate electrolyte and a metal or semiconductor material serving as the counter electrode.[9–11] However, photoelectrodes in PEC water splitting based on metal oxide semiconductors, *i.e.*, TiO₂, ZnO, are challenging due to their narrow visible light absorption, unfavorable band positions, low charge mobilities, and less photo-stability, making it challenging to achieve efficient overall performance.[12] To enhance the separation of photogenerated carriers and expand the absorption of active light, it is advantageous to combine various metal oxides into different hetero-structures; therein, the type-II heterojunction is a typical case.[13–15] In type-II heterojunctions, the movement of holes and electrons occurs in opposite directions, enabling effective separation and transfer of charge carriers at the interface.[16]

Zinc oxide (ZnO ∼3.37 eV) is a semiconductor that exhibits excellent efficiency for PEC due to its CB position (E_{CB}) at −0.22 V *vs.* NHE, which indicates an opposing alignment relative to the favorable water reduction potential for the hydrogen evolution half-reaction (HER).[17,18] However, ZnO is responded to UV light excitation, which constitutes only 5% of the total solar energy spectrum.[19] Besides, the high photo-corrosion of ZnO

[a]Advanced Materials and Applications Research Group (AMA), HUTECH University, 475A Dien Bien Phu Street, Binh Thanh District, Ho Chi Minh City, 700000, Vietnam. E-mail: pv.viet@hutech.edu.vn

[b]University of Science, Ho Chi Minh City, Vietnam

[c]Vietnam National University Ho Chi Minh City, Linh Trung Ward, Thu Duc City, Ho Chi Minh City, Vietnam

[d]Institute of Materials Science, Vietnam Academy of Science and Technology, 18 Hoang Quoc Viet, Hanoi, Vietnam

under UV irradiation in aqueous environments also limits its widespread application.[20] Meanwhile, cobalt oxide (Co_3O_4) possesses two distinct optical band gaps that correspond to the energy state transitions of $O^{2-} \rightarrow Co^{3+}$ (~1.4 eV) and $O^{2-} \rightarrow Co^{2+}$ (~2.1 eV), leading to the enhancement of electron charge transfer.[21,22] The nanostructured Co_3O_4 films remained stable during chronopotentiometry tests in acidic and alkaline environments.[23,24] By constructing a Co_3O_4 layer onto the ZnO layer, the exposure of ZnO to the aqueous solution can be prevented, thereby mitigating its photo-corrosion. The rapid recombination rate of photoexcited electron–hole pairs is a notable drawback observed in many individual semiconductor materials. As a result, recent studies proposed that the integration of both broad-band gap and narrow-band gap materials or metal-semiconductors could lead to efficient heterojunctions.[25]

The fabrication of ZnO and Co_3O_4 p–n junctions has gained attention due to the unique properties of these materials. ZnO, excited by UV light, is employed as the n-type material, while Co_3O_4, which can absorb visible light, is the p-type material.[26] These junctions have shown promising applications in photocatalytic CO_2 reduction,[27] degradation of dyes,[28] and photoelectrochemical water oxidation.[29] To fabricate a Co_3O_4/ZnO p–n heterojunction, ZnO nanomaterials and Co_3O_4 nanoparticles were synthesized by many methods, for instance, a combination of the vapor–liquid–solid method at 800 °C and the hydrothermal method for 10 hours at 200 °C.[30] In another approach, the Co_3O_4–ZnO core–shell structure was synthesized by hydrothermally fabricating pristine Co_3O_4 nanowires on an FTO glass substrate at 110 °C for 5 hours and the Co_3O_4–ZnO film was obtained by annealing in air at 500 °C for 15 minutes using a muffle furnace.[31] In another study, Markhabayeva et al.[32] employed a combination of spin coating and chemical bath deposition, with two annealing stages at each step to synthesize the ZnO/Co_3O_4 on ITO. In contrast to alternative synthesis methods that involve expensive equipment, high temperatures, and long synthesis time, the Co_3O_4/ZnO p–n heterojunction was successfully fabricated using the electrodeposition method. This approach not only saves time but also requires a simple equipment setup. The ZnO layer was electrodeposited for 8000 seconds, and the $Co(OH)_2$ layer was electrodeposited for 360 seconds. The Co_3O_4/ZnO junction was annealed in an ambient environment at 300 °C for 3 hours.[33]

In this study we synthesized a photoelectrode Co_3O_4/ZnO/FTO specifically for HER applications. The influence of deposition time on the electrode properties was investigated. The fabricated electrode's characteristics were evaluated using XRD (X-ray diffraction), FTIR (Fourier-transform infrared spectroscopy), SEM-EDX (scanning electron microscopy with energy-dispersive X-ray spectroscopy), DRS (Diffuse Reflectance Spectroscopy), and PL (photoluminescence)—various techniques were used to assess electrochemical properties, including LSV (Linear Sweep Voltammetry) and Mott–Schottky plot. The photoelectrochemical efficiency was also determined by measuring the photocurrent density under simulated solar light conditions. Finally, the mechanism of the hydrogen evolution reaction using the Co_3O_4/ZnO/FTO photocathode under simulated solar light illumination is proposed.

2. Experimental

2.1. Chemicals

Co_3O_4/ZnO/FTO materials were fabricated using zinc nitrate ($Zn(NO_3)_2 \cdot 6H_2O$, Xilong, China), pure zinc sheet (99.99%), commercial FTO glass (13–15 Ω sq^{-1}), cobalt nitrate ($Co(NO_3)_2 \cdot 6H_2O$, Xilong, China), deionized (DI) water (Milli-Q, 18 MΩ cm), ethylene glycol ($C_2H_6O_2$) and acetone (C_3H_6O). In addition, sodium sulfate (Na_2SO_4) was used in electrochemical measurements.

2.2. Synthesis of Co_3O_4/ZnO/FTO
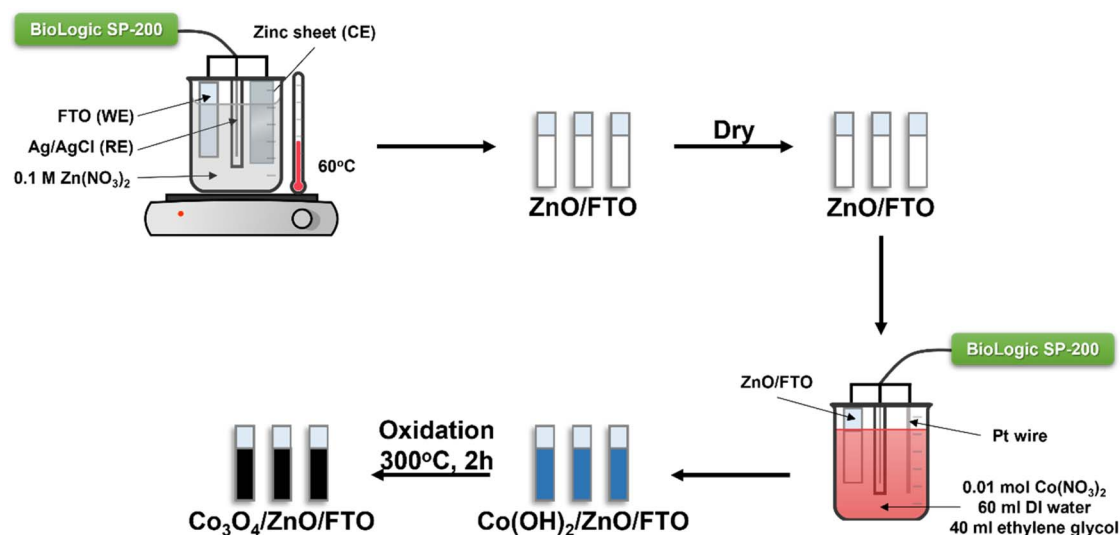
A two-step fabrication process was used to synthesize Co_3O_4/ZnO/FTO materials. In the first step ZnO was synthesized by electrochemical deposition in a three-electrode system from a 0.1 M zinc nitrate electrolyte solution. FTO glass, a pure zinc sheet (99.99%), and an Ag/AgCl electrode (in a saturated KCl solution) were used as the working electrode (WE), counter electrode (CE), and reference electrode (RE), respectively. FTO glass with a surface resistivity of about 13–15 Ω sq^{-1} was cut into samples of 1.0 cm × 2.0 cm, cleaned with acetone and DI water sequentially in an ultrasonic bath for 20 minutes, then dried. The electrolyte solution was maintained at 60 °C throughout the experiment. The deposition time was 5 minutes with a constant voltage of −1.0 V (vs. Ag/AgCl). After deposition, the ZnO/FTO film was washed with DI water and dried in an oven.

In the second step, the previously prepared ZnO-coated FTO glass was used to continue the deposition of $Co(OH)_2$ at room temperature. The electrochemical three-electrode system at this time consisted of ZnO-coated FTO glass, a platinum (Pt) wire, and an Ag/AgCl electrode (in a saturated KCl solution) used as the working electrode, counter electrode, and reference electrode, respectively. The electrolyte solution contained 0.01 mol $Co(NO_3)_2 \cdot 6H_2O$, 60 ml DI water, and 40 ml ethylene glycol. The deposition process was carried out at a constant voltage of −1.0 V (vs. Ag/AgCl) with the respective survey times of 2, 4, 6, and 8 minutes. Then, $Co(OH)_2$/ZnO/FTO was dried and annealed at 300 °C for 2 hours with a constant heating rate of 3 °C min^{-1} to form Co_3O_4/ZnO/FTO. The samples are denoted as Co_3O_4-2/ZnO/FTO, Co_3O_4-4/ZnO/FTO, Co_3O_4-6/ZnO/FTO, and Co_3O_4-8/ZnO/FTO corresponding to Co_3O_4 deposition times of 2, 4, 6, and 8 minutes, respectively. The flowchart of the material synthesis process is described in Scheme 1.

2.3. Characterization of materials

The crystal structures of the ZnO/FTO and Co_3O_4/ZnO/FTO samples were characterized by XRD using a Bruker D8 Advanced instrument with Cu Kα radiation ($\lambda = 1.5406$ Å) as the X-ray source, an electron acceleration voltage of 45 kV and a current of 45 mA. The instrument was set to scan from 10° to 80° with a scan rate of 0.02° s^{-1}. For FTIR measurements, a JASCO FT/IR-4700 was used to identify the vibrational features of the material's surface functional groups. The sample and KBr mixture were compressed into a round pellet with a diameter of 1 cm and a mass ratio of sample/KBr of 1/300. The compressed

Scheme 1 Schematic illustration of the preparation of $Co_3O_4/ZnO/FTO$.

pellets were then placed in the instrument for analysis; the IR signal was scanned from wavenumber 4000 cm^{-1} to 400 cm^{-1} with a wavenumber resolution of 1 cm^{-1}. The surface morphology of the material was investigated by SEM using a JEOL JSM-IT500. Before observing the SEM images, the electrodes were placed in the measurement chamber with an accelerating voltage of 20 kV. JSM-IT500 was also used for EDX mapping to obtain the elements present in the sample and the weight percentage of each element. The optical properties of the material were determined from the DRS spectrum and the Tauc plot. The DRS method was performed on a JASCO V-770 spectrophotometer in the wavelength range from 300 to 800 nm. The PL spectrum was measured using a Cary Eclipse Fluorescence Spectrophotometer with an excitation wavelength of 300 nm.

Photoelectrochemical measurements, including LSV, photocurrent density, Mott–Schottky, and EIS of the synthesized samples, were performed using a Biologic SP-200 potentiostat and were carried out in a three-electrode system. The working electrode was the investigated material, the counter electrode was a Pt wire, and the Ag/AgCl electrode (in saturated KCl solution) was the reference electrode. All electrochemical experiments were performed at room temperature in 0.1 M Na_2SO_4 solution (pH ~7). LSV measurements were performed at a scan rate of 10 mV s^{-1}. The potential was linearly scanned with time while the current was measured and recorded through a reversible hydrogen electrode (V $vs.$ RHE) according to eqn (1):

$$E_{RHE} = E_{Ag/AgCl} + 0059 \times pH + E^0_{Ag/AgCl} \qquad (1)$$

In this equation, E_{RHE} is the potential concerning the reversible hydrogen electrode, $E_{Ag/AgCl}$ is the experimentally measured potential, and $E^0_{Ag/AgCl} = 0.197$ V at 25 °C.

The photocurrent density was determined using a solar simulator device from Abet Technologies. During the measurement, the applied voltage was kept constant at 0.80 V

($vs.$ RHE), the light window was turned on and off every 60 seconds per cycle, and the measurement was repeated seven times. Furthermore, Mott–Schottky measurements were performed at a fixed frequency of 100 kHz to obtain the material's conduction band. Electrochemical impedance spectroscopy (EIS) measurements were carried out with a frequency range from 100 kHz to 0.1 Hz and an amplitude of 10 mV.

3. Results and discussion

3.1. Structural and morphological properties

The synthesized samples' structural and crystalline characteristics were analyzed by XRD and FTIR (Fig. 1). The XRD patterns of ZnO/FTO and $Co_3O_4/ZnO/FTO$ samples are shown in Fig. 1a. Accordingly, the characteristic diffraction peaks of ZnO from the standard pattern (JCPDS #36-1451) are observed at diffraction angles (2θ) of 31.8°, 34.3°, 36.5°, 47.6°, 57.2°, 63.2°, 67.9°, 69.0°, and 72.7°, corresponding to the (100), (002), (101), (102), (110), (103), (112), (201), and (004) planes, respectively. The XRD results of the synthesized ZnO sample are consistent with the standard pattern, indicating that ZnO has been successfully deposited on the FTO substrate with a hexagonal wurtzite crystal structure.[33] The prominent diffraction peaks of the ZnO sample corresponding to the (100), (002), and (101) planes have strong intensities, indicating that the formed material has a relatively good crystallinity. In addition, the diffraction peaks in the XRD patterns of $Co_3O_4/ZnO/FTO$ samples synthesized with different electrolysis times all match well with the standard diffraction pattern of ZnO (JCPDS #36-1451), indicating that ZnO has been successfully deposited on the FTO substrate in all samples. It was observed that the intensity of the ZnO (101) peak gradually increases, and the intensity of the (002) peak gradually decreases with increasing Co_3O_4 deposition time. This was explained by the diffraction peak corresponding to the (311) plane of Co_3O_4 in the standard pattern (JCPDS #42-1467), which is the strongest. However, the position of the diffraction peak
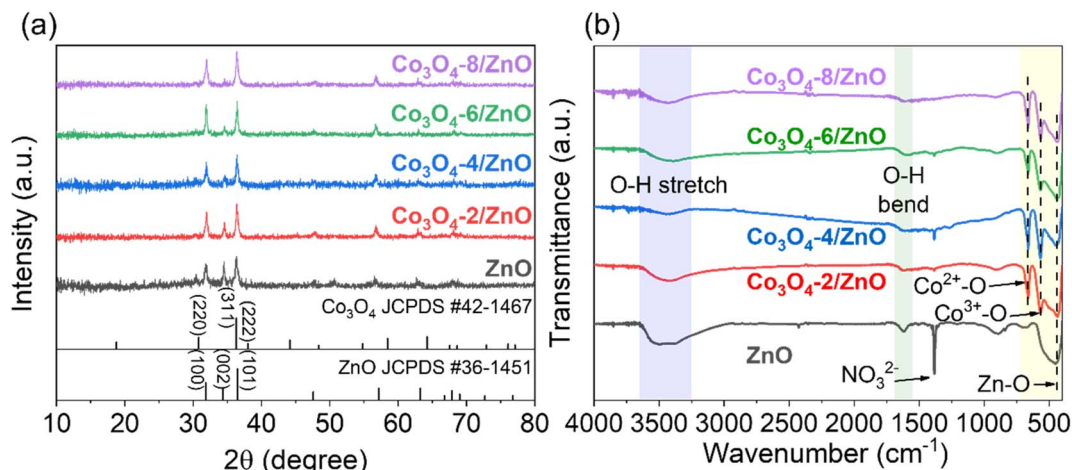
Fig. 1 XRD patterns (a) and FTIR spectra (b) of ZnO/FTO and Co$_3$O$_4$/ZnO/FTO samples.

corresponding to the (311) plane of Co$_3$O$_4$ was overlapped with that of the ZnO (101) peak. The overlap of the two planes explains the change in the symmetry of the peak at this position, and when the electrolysis time increases, the amount of Co$_3$O$_4$ on ZnO will increase, leading to increased diffraction intensity. This result partly shows the successful deposition of Co$_3$O$_4$ on ZnO. However, the XRD patterns of all the samples did not show any clear diffraction peaks of Co$_3$O$_4$. Therefore, the FTIR method was performed to verify the presence of Co$_3$O$_4$ (Fig. 1b). In detail, the appearance of the bands at a wavelength of approximately 3440 cm^{-1} and 1600 cm^{-1} can be attributed to the stretching and bending vibrations of the O–H bond, which may be caused by adsorbed water on the material's surface or by atmospheric humidity.[34] The signal at a wavelength of approximately 455 cm^{-1} is characteristic of the stretching vibration of the Zn–O bond.[35] At a wavelength of 572 cm^{-1} and 664 cm^{-1}, two characteristic peaks appear that correspond to the stretching vibrations of the two bonds: Co(III)–O when the Co^{3+} ions are in an octahedral coordination state and Co(II)–O when the Co^{2+} ions are in a tetrahedral coordination state.[36] These characteristic peaks are present in all Co$_3$O$_4$/ZnO/FTO samples, demonstrating the successful synthesis of Co$_3$O$_4$ on the ZnO structure. At the same time, these are also two characteristics of the spinel structure of Co$_3$O$_4$. This result again confirms the successful synthesis of Co$_3$O$_4$ on the ZnO/FTO substrate. In addition, the sharp peak at around 1398 cm^{-1} is considered the vibrational signal of the NO$_3^-$ radical. This is likely since both the syntheses of ZnO and Co$_3$O$_4$ use metal nitrate salts as the electrolyte solution, leading to residual NO$_3^-$ on the material's surface. It is also noted that because the ZnO synthesis process only involves drying without requiring high-temperature annealing, the amount of NO$_3^-$ on the ZnO sample is the highest, leading to the strongest absorption intensity.

The surface morphology of ZnO synthesized by electrochemical deposition on the FTO substrate was observed by SEM. Fig. 2a is a low magnification SEM image (2000×) showing that the surface image of the ZnO film developed uniformly on the FTO substrate. Fig. 2b is a high magnification SEM image (20

000×), indicating that the ZnO obtained has a thin nanoplate structure arranged closely together. SEM also provided the surface morphology of the Co$_3$O$_4$/ZnO/FTO sample, as in Fig. 2c and d. In detail, the Co$_3$O$_4$ layer on top has a nanopetal structure that is intertwined and developed uniformly on the ZnO substrate, similar to previous reports on electrochemically deposited Co$_3$O$_4$.[37] Thus, based on the SEM images of the samples, it can be concluded that the Co$_3$O$_4$/ZnO bilayer material with a nanopetal/nanoplate structure on the FTO substrate was successfully synthesized by the electrochemical deposition method with high coverage and uniformity.

In addition, EDX was employed to investigate the elemental composition and potential presence of impurities on the surface of both the ZnO/FTO and Co$_3$O$_4$/ZnO/FTO samples. The EDX mapping of the ZnO/FTO sample is shown in Fig. 2e–i. The appearance of Zn and O element peaks (Fig. 2e) has proved the successful synthesis of ZnO by electrochemical deposition. In addition, there are also peaks of other elements, such as Sn and F, which are thought to be from the FTO substrate. The mapping images (Fig. 2f–i) show that the elements Zn (red) and O (blue) appear mainly in the ZnO deposition area; at the same time, the uniform distribution of the mapping once again confirms that ZnO was deposited successfully and uniformly on the FTO substrate. Based on EDX mapping of the Co$_3$O$_4$/ZnO/FTO sample (Fig. 2j–n), the existence of the elements Co, Zn, and O is shown, which implies the successful synthesis of Co$_3$O$_4$ nanopetals on ZnO/FTO by the electrochemical deposition/annealing method. In addition, no other elements were identified, suggesting that the purity of the synthesized sample is high.

3.2. Optical properties

To evaluate the optical properties of the materials after fabrication, the DRS spectra of the synthesized Co$_3$O$_4$/ZnO samples and the Tauc plots are calculated from the DRS spectra of ZnO, Co$_3$O$_4$-2, and Co$_3$O$_4$-2/ZnO samples, which are shown in Fig. 3. The Co$_3$O$_4$/ZnO samples were synthesized with different deposition times (Fig. 3a). For samples with Co$_3$O$_4$ deposition times
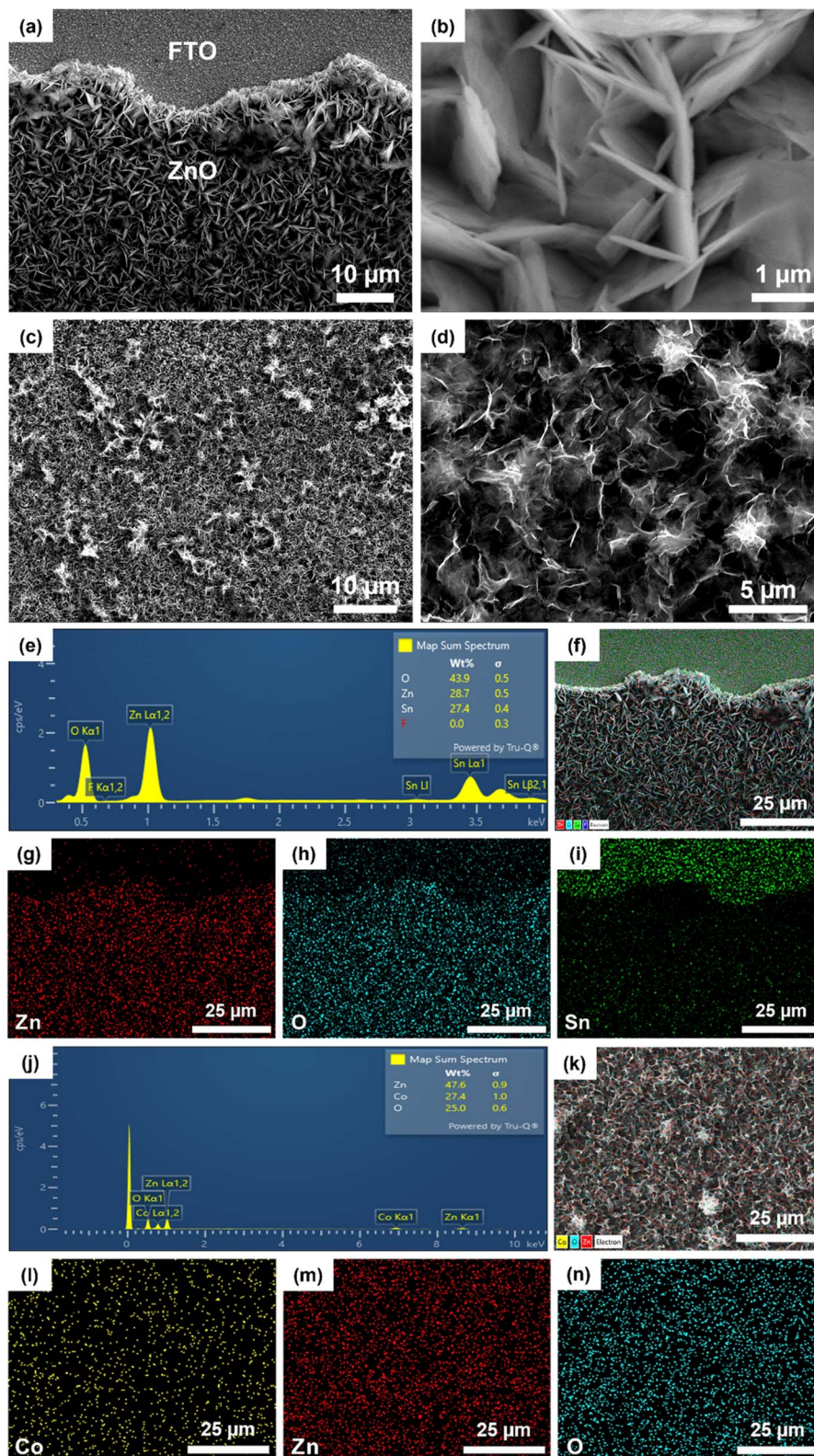
Fig. 2 SEM images of the ZnO/FTO sample at magnifications (a) 2000×, (b) 20 000×; SEM images of the Co_3O_4/ZnO/FTO sample at magnifications (c) 2000×, (d) 5000×; EDX-mapping of ZnO/FTO (e–i) and Co_3O_4/ZnO/FTO (j–n).

from 2 to 4 minutes, clear absorption peaks of ZnO at 310 nm in the UV region are observed. Meanwhile, the DRS spectra of the samples with Co_3O_4 deposition times of 6 and 8 minutes show two absorption peaks at 380 nm and 678 nm, respectively, confirming the cubic spinel structure of Co_3O_4. The enhancement of the characteristic peaks of Co_3O_4 is explained by
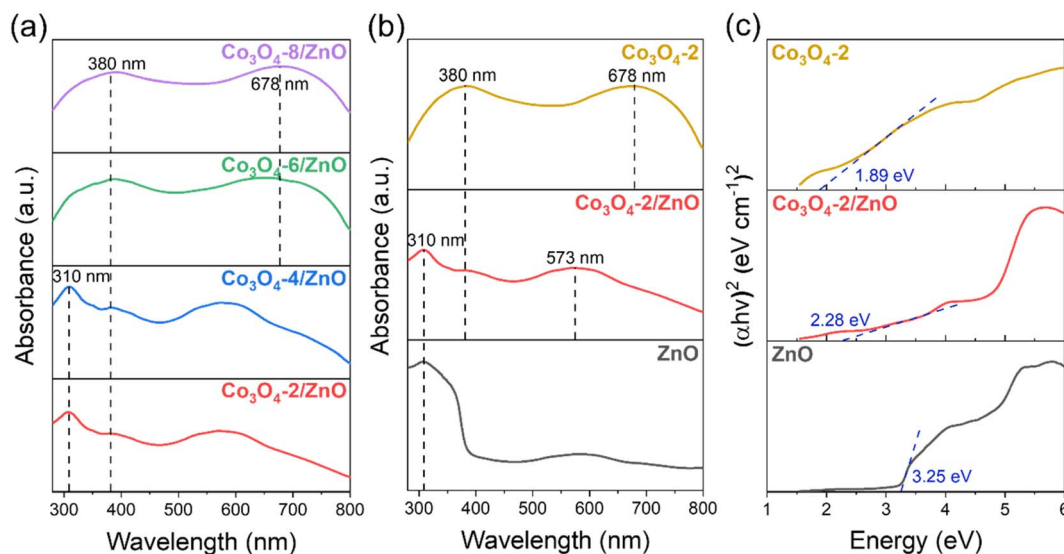
Fig. 3 DRS spectra of the synthesized Co_3O_4/ZnO samples with different deposition times (a); DRS spectra (b) and Tauc plots (c) of synthesized ZnO, Co_3O_4-2, Co_3O_4-2/ZnO samples.

increasing the deposition time, causing the thickness of Co_3O_4 to increase, and losing the typical signal of the ZnO layer. The absorption peak at 380 nm represents the charge transfer of $O^{2-} \rightarrow Co^{2+}$, and the absorption peak at 678 nm represents the charge transfer of $O^{2-} \rightarrow Co^{3+}$.[38] This shows that as the Co_3O_4 deposition time increases, the Co_3O_4 layer becomes thicker and dominates the material, leading to the inability to record the absorption signal of ZnO. The results from the DRS spectrum also confirmed the successful synthesis of ZnO and Co_3O_4 on FTO substrates by electrochemical deposition. In addition, a Co_3O_4-2 sample was directly synthesized on the FTO substrate (same process as before with a deposition time of 2 minutes) to compare the material's band gap value before and after the combination. The DRS spectra of the ZnO, Co_3O_4-2, and Co_3O_4-2/ZnO samples (Fig. 3b) were converted to Tauc plots and are shown in Fig. 3c. According to the results obtained from the Tauc plot in Fig. 3c, the band gaps of ZnO, Co_3O_4-2, and Co_3O_4-2/ZnO are 3.25 eV, 1.89 eV, and 2.28 eV, respectively. This shows that the combination of the two materials has created a structure with an intermediate band gap value, lying between the original values of ZnO and Co_3O_4. This band gap value corresponds to the energy of visible light, so Co_3O_4/ZnO photoelectrodes can receive more energy from visible light than ZnO photoelectrodes. The narrowing of the band gap value in the Co_3O_4/ZnO material compared to ZnO can be predicted that the photoelectrochemical water splitting ability of the ZnO material can be enhanced when combined with Co_3O_4 compared to when in a separate state.

PL spectra are used to determine the separation ability and recombination rate between photogenerated electrons and holes in semiconductor material structures. Fig. 4 shows the PL spectra of the synthesized ZnO, Co_3O_4-2, and Co_3O_4-2/ZnO samples at room temperature. An emission band with broad characteristics was detected at a wavelength of 550 nm in the ZnO layer. This observation can be attributed to defects,

specifically singly ionized oxygen vacancies.[39,40] Upon combining the Co_3O_4-2 with the ZnO layer, a noticeable redshift of the emission peak to 563 nm was observed. This suggests that combining Co_3O_4-2 and the ZnO layer on FTO can enhance visible light absorption, thereby enabling more efficient PEC water splitting.

The emission intensity in the Co_3O_4-2 and Co_3O_4-2/ZnO structures is much lower than in pure ZnO. This indicates the better separation and reduced recombination of charge carriers in the Co_3O_4-2 structure and the Co_3O_4-2/ZnO heterojunction than in ZnO. The difference in emission intensity in the PL spectrum can be attributed to the reduced recombination and extended lifetime of photogenerated electron–hole pairs. This implies that Co_3O_4 has the ability to inhibit the recombination of electrons and holes in ZnO, thereby helping to enhance the
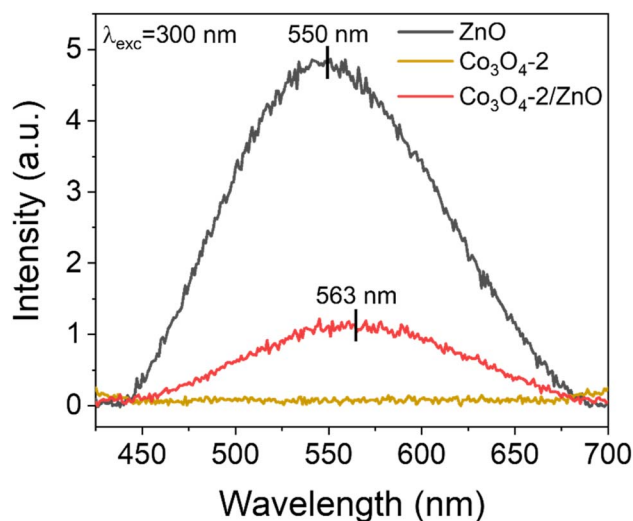

Fig. 4 PL spectra of ZnO, Co_3O_4-2, and Co_3O_4-2/ZnO samples.

photocatalytic effects of the material. Moreover, the emission peak at 550 nm of ZnO is typically assigned to the oxygen vacancy defect states of ZnO. Meanwhile, the typical emission peak of Co_3O_4 located at 563 nm could be assigned to the band-to-band emission of Co_3O_4, which is in agreement with the DRS result analysis in Fig. 3c.

3.3. Photoelectrochemical water splitting activity

The electrochemical water splitting activity of the material is shown by the LSV results (Fig. 5a and b). Co_3O_4/ZnO samples with different Co_3O_4 deposition times were subjected to LSV (HER) measurements to evaluate the HER activity. The LSV curves were recorded at a scan rate of 10 mV s^{-1} in 0.1 M Na_2SO_4 electrolyte solution. In addition, FTO glass and ZnO/FTO (same size) samples were also prepared for LSV measurements for comparison. Fig. 5a shows that the Co_3O_4-2/ZnO, Co_3O_4-6/ZnO, and Co_3O_4-8/ZnO samples have the lowest onset potential, which is close to each other (−0.7 V). However, the Co_3O_4-2/ZnO sample has the highest current density (127.7 mA cm^{-2}) compared to the other samples. All the material samples used as catalytic electrodes showed a high current density at more negative potentials, and the LSV curves were also linear and straight, indicating that this material is quite stable in the electrochemical water splitting reaction to generate hydrogen.

Similarly, LSV measurements were also performed to evaluate the material's electrochemical water-splitting activity via the oxygen evolution reaction (OER). Fig. 5b is a characteristic LSV curve for the OER reaction performed in 0.1 M Na_2SO_4 electrolyte recorded at a scan rate of 10 mV s^{-1}. The results show that the Co_3O_4-2/ZnO sample has the lowest onset potential (0.82 V) and the smallest overpotential of 470 mV at a current density of 10 mA cm^{-2}. Based on the two LSV (HER and OER) results, it can be concluded that the Co_3O_4-2/ZnO material exhibits the best electrochemical water-splitting activity. Therefore, the optimal deposition time for Co_3O_4 on ZnO is 2 minutes. It was also found that the deposition of Co_3O_4 on the surface of ZnO can increase the efficiency of the electrochemical water-splitting reaction.

Non-illuminated and illuminated LSV measurements were performed using a solar simulator for ZnO/FTO and Co_3O_4-2/ZnO/FTO samples to investigate the photoelectrochemical activity of water splitting. LSV curves were also recorded at a scan rate of 10 mV s^{-1} in 0.1 M Na_2SO_4 electrolyte solution. The LSV results for the hydrogen evolution reaction of the materials are shown in Fig. 5c. The results show that both the ZnO and Co_3O_4-2/ZnO samples have lower onset and over-potentials when illuminated than when not illuminated. The photocurrent density of the illuminated samples is also higher
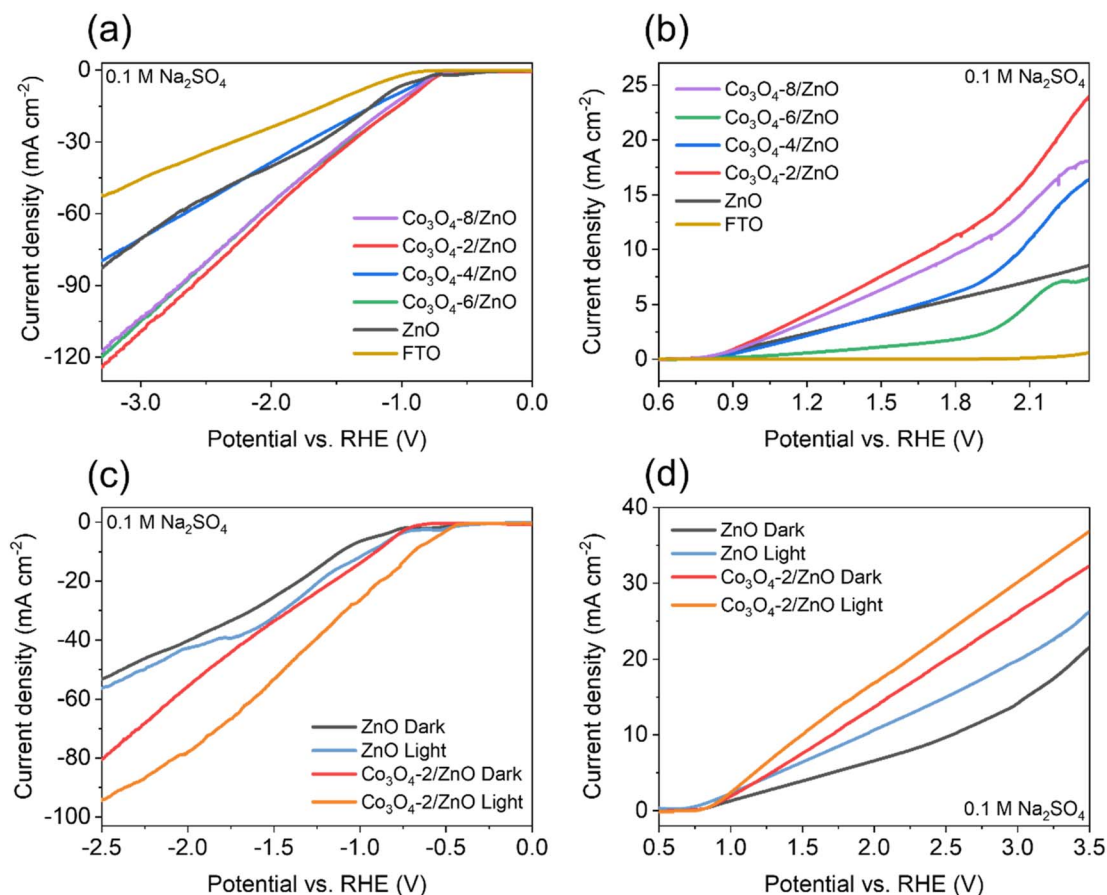

Fig. 5 HER (a) and OER (b) curves of FTO, ZnO and Co_3O_4/ZnO samples; HER (c) and OER (d) curves of ZnO and Co_3O_4-2/ZnO samples under the illuminated and non-illuminated conditions.

at the same applied potential. Specifically, the illuminated Co_3O_4-2/ZnO sample has an onset potential of -0.5 V and an overpotential of 670 mV, which are lower than the onset potential of -0.7 V and overpotential of 900 mV of the non-illuminated sample. The LSV (OER) curves are shown in Fig. 5d. The LSV results show that, although the onset potential of the illuminated samples shows a slight decrease, when illuminated, both the ZnO and Co_3O_4-2/ZnO samples give higher current density and lower overpotential. The illuminated ZnO and Co_3O_4-2/ZnO samples have overpotentials of 700 mV and 260 mV, respectively, while under the non-illuminated conditions, the corresponding overpotential values are 1310 mV and 470 mV. From the illuminated LSV results, it can be concluded that light plays an important role in increasing the water splitting efficiency of the material. When light is irradiated onto the material, a higher water splitting current density is observed than in the non-illuminated state (under dark conditions). This suggests that light has excited the electrons in the material, giving them sufficient energy to participate in the water-splitting reaction, thereby increasing the number of electrons participating in the reaction and making the process more efficient.

The light-chopped LSV and photocurrent density measurements were performed to determine the material's light-responsive ability, and the results are shown in Fig. 6.

The optimized Co_3O_4-2/ZnO and ZnO electrodes were utilized in the chopped LSV experiment to investigate the photoresponse during on–off cycling in the voltage range of 0.5 to 1.5 V vs. RHE. The results, shown in Fig. 6a, demonstrate that the chopped LSV curves were consistently similar to the continuous dark and light LSV curves. Additionally, all electrodes exhibited rapid and reproducible photoresponse throughout each on–off cycle. To assess the enhancement of the Co_3O_4/ZnO heterojunction compared to ZnO, the steady-state photocurrent was measured at 0.8 V vs. RHE. The results in Fig. 6b show that the photocurrent density of the Co_3O_4-2/ZnO sample is 1.4 times higher than that of the ZnO sample, from which it can be concluded that the ZnO material has a lower photo-response ability under the action of solar light than the

Co_3O_4/ZnO material. This may be because ZnO has a large band gap, so it can only absorb energy from the UV region. In contrast, the combined sample may have a smaller band gap, resulting in more light energy being obtained (under the same illumination conditions). At the same time, the light energy conversion efficiency of the ZnO sample also decreases faster than the Co_3O_4/ZnO sample after seven cycles, which shows that the combined material has higher stability and photoelectric efficiency than the ZnO material.

Table 1 shows the comparison of different PEC electrodes on the FTO substrate. The electrode fabrication process, involving the electrodeposition of ZnO for 5 minutes and $Co(OH)_2$ for 2 minutes, followed by a 3 hours annealing step at 300 °C, offers several advantages. It is a time-saving method that requires simple equipment and operates at a lower temperature than previous studies. Furthermore, the current density at 1.23 V under the same illumination conditions was 5.9 mA cm^{-2}. This notable current density is higher when compared to other PEC electrodes based on FTO substrates.[41–45]

The Mott–Schottky method evaluates synthesized material samples' carrier density and electronic conductivity type (p-type or n-type). The type of semiconductor is determined by the slope of the Mott–Schottky plot, with a positive slope indicating an n-type semiconductor and a negative slope indicating a p-type semiconductor. Additionally, Mott–Schottky measurements have been used to determine the materials' conduction band energy level (E_{CB}) before combination. A Mott–Schottky plot is a graph of the inverse square of the capacitance and the resistance components of the impedance versus the applied potential (C^{-2} vs. E) according to eqn (2).

$$\frac{1}{C_{sc}^{2}} = \frac{2}{e\varepsilon\varepsilon_0 N}\left(E - E_{fb} - \frac{kT}{e}\right) \quad (2)$$

where C_{sc} is the capacitance of the space charge region, ε the relative dielectric constant of the semiconductor, ε_0 the vacuum permittivity of the free space, N is the donor or the acceptor density, E the electrode potential, E_{fb} the flat band potential, k is the Boltzmann constant, and T the absolute temperature. The plot of $1/C^2$ against the applied voltage will show a tangent that
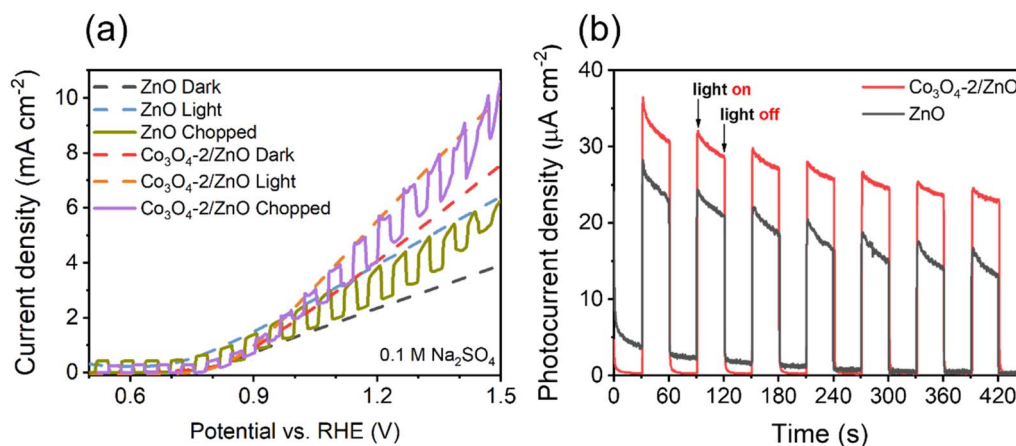

Fig. 6 Light-chopped LSV curves (a) and photocurrent density response (b) of ZnO and Co_3O_4-2/ZnO samples.

Table 1 Comparison of PEC electrode performance on FTO substrates under LSV illumination

No.	Material	Synthesis process	Electrolyte	Current density at 1.23 V vs. RHE (mA cm^{-2})	Illumination conditions	Ref.
1	BiVO$_4$/WO$_3$/SnO$_2$	SnO$_2$ film was initially deposited on the FTO/glass substrate WO$_3$ was deposited on top of the SnO$_2$ film BiVO$_4$ nanoparticle film was deposited using the spin coating technique	0.5 M phosphate buffer	3.1	Simulated solar light illumination (100 mW cm^{-2})	41
2	Fe$_2$O$_3$/WO$_3$ NRs	Deposition of WO$_3$ onto FeOOH NRs, then coating on FTO glass and annealing at 450 °C for 4 h	0.1 M Na$_2$SO$_4$	1.03	Xe 300 W lamp with AM 1.5G	42
3	ZnFe$_2$O$_4$/α-Fe$_2$O$_3$	α-Fe$_2$O$_3$ on FTO: hydrothermal 120 °C for 6 h then annealed at 550 °C for 2 h ZnFe$_2$O$_4$/α-Fe$_2$O$_3$ nanorods: depositing ZnO film onto the α-Fe$_2$O$_3$ of 430 cycles, annealed at 550 °C for 10 h, then washed with 1 M NaOH solution for 10 h to remove ZnO	1 M NaOH	0.29	AM 1.5G illumination (100 mW cm^{-2})	43
4	WO$_3$/g-C$_3$N$_4$	WO$_3$/g-C$_3$N$_4$ heterojunction was prepared by electrophoretic deposition at 10 V then annealed at 350 °C for 2 h	0.5 M Na$_2$SO$_4$	0.22	Chopped light illumination (AM 1.5G, 100 mW cm^{-2})	44
5	BiVO$_4$/ZnCo$_2$O$_4$	BiVO$_4$ nanoworms: growth of BiOI nanoflake structure by electrodeposition and then transformation of BiOI nanoflakes into BiVO$_4$ nanoworms by chemical and calcination methods ZnCo$_2$O$_4$ nanoparticles: hydrothermal at 20 °C for 12 h then dry 80 °C for 12 h	0.5 M Na$_2$SO$_4$	1.92	Xe 150 W lamp with AM 1.5G	45
6	Co$_3$O$_4$/ZnO/FTO	Electrochemical deposition ZnO 5 min and Co$_3$O$_4$ 2 min Annealing at 300 °C for 2 h	0.1 M Na$_2$SO$_4$	5.9	150 W Xe lamp	This work

cuts the horizontal axis, the point of intersection will indicate the value of E_{fb}, also known as the E_{CB} of the material.

The Mott–Schottky plot of the ZnO material presented in Fig. 7a shows a positive slope, which indicates that ZnO is an n-type semiconductor. The results show that the conduction band energy level of the ZnO sample is −0.22 V (*vs.* NHE). This result is consistent with the previously reported values of ZnO.[46] Upon application of external reverse bias to a p-type semiconductor, the depletion region experiences an expansion, consequently leading to an increase in the space-charge capacitance and a subsequent decrease in the value of $1/C^2$.[47] As a result, the negative slope in the Mott–Schottky plot of the Co_3O_4 sample (Fig. 7b) provides conclusive evidence for its p-type conductivity, consistent with the presence of majority holes as charge carriers. In addition, the Mott–Schottky results also show that the conduction band energy level of the Co_3O_4 material is 0.74 V (*vs.* NHE).

To study the charge-transport behavior existing between the electrode and the electrolyte junction, the data obtained from EIS measurements were analyzed using a simple Randles equivalent circuit (Fig. 7c and d). In this circuit, R_1 is the solution resistance, R_2 (R_{CT}) is the charge transfer resistance, Q_2 is the double layer capacitance, and W is the Warburg impedance. The diameter of the semicircle in the Nyquist plot of EIS is related to the charge transfer resistance and the electron–hole separation efficiency. Therefore, a smaller semicircle diameter indicates a lower charge transfer resistance, *i.e.*, a higher charge transfer efficiency. Based on the EIS results shown in Fig. 7c, the semicircle diameter in the Nyquist plot of the ZnO sample is smaller than that of the Co_3O_4 sample. This implies that the electrical resistivity for charge transport for the n-type semiconductor ZnO is lower than that for the p-type semiconductor Co_3O_4, and thus promotes the kinetics of surface reactions on ZnO.

From the conduction band energy level E_{CB}, combined with the above band gap values, the energy diagram characteristic of the photoelectrochemical water splitting ability of the material is shown in Fig. 8. The improvement in the photo-electrochemical activity of ZnO for the water splitting reaction by adding Co_3O_4 is mainly due to two main reasons. First, the narrow band gap of Co_3O_4 helps to reduce the band gap value of the Co_3O_4/ZnO material compared to ZnO alone. Second, the p–n junction formed at the interface between the Co_3O_4 layer and the ZnO layer increases the concentration of electrons involved in the photoelectrochemical water splitting process.

As illustrated in Fig. 8a, the valence bands (VBs) of Co_3O_4 and ZnO are 2.63 V/NHE and 3.03 V/NHE, respectively, the CBs of Co_3O_4 and ZnO are 0.74 V/NHE and −0.22 V/NHE, respectively. After combining ZnO, an n-type semiconductor with a band gap of 3.25 eV, with Co_3O_4, which can be considered a p-type semiconductor with a band gap of 1.89 eV, the energy levels of Co_3O_4 shift up, while those of ZnO shift down until the Fermi levels of Co_3O_4 and ZnO reach equilibrium. Therefore, p–n junctions are formed at the interface between ZnO and Co_3O_4

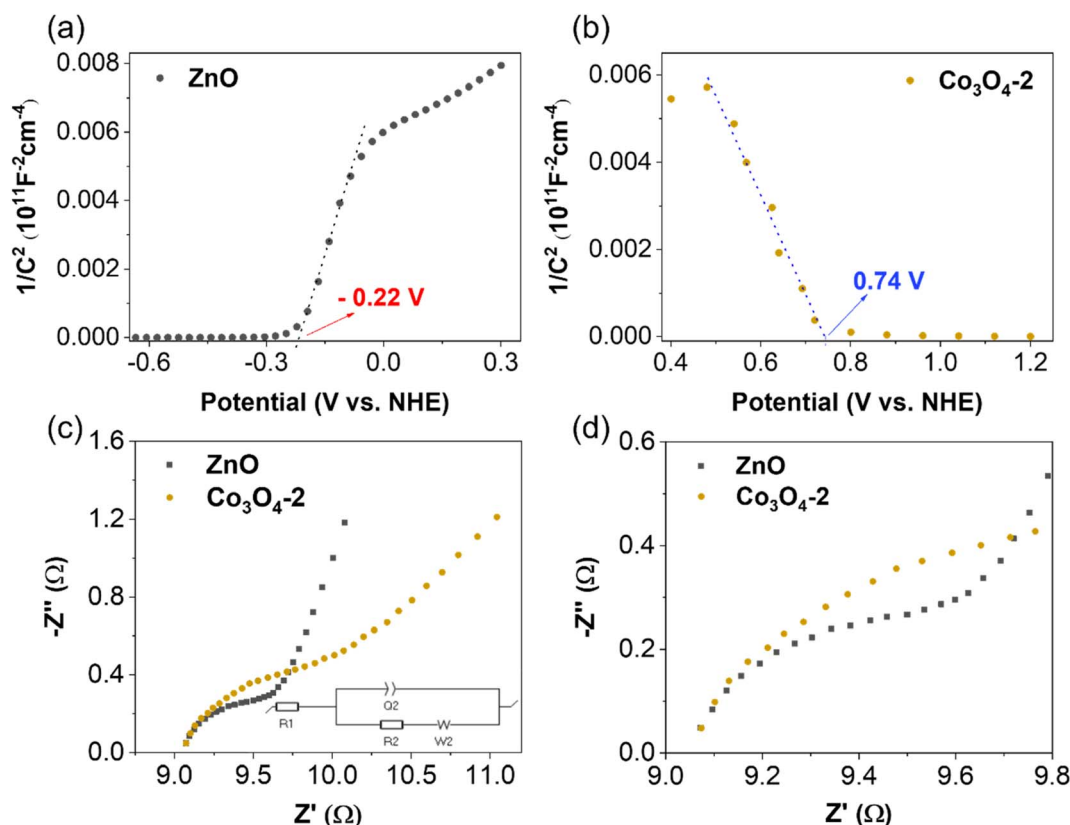**Fig. 7** Mott–Schottky plots of (a) ZnO, (b) Co_3O_4-2 and (c and d) EIS Nyquist plots.

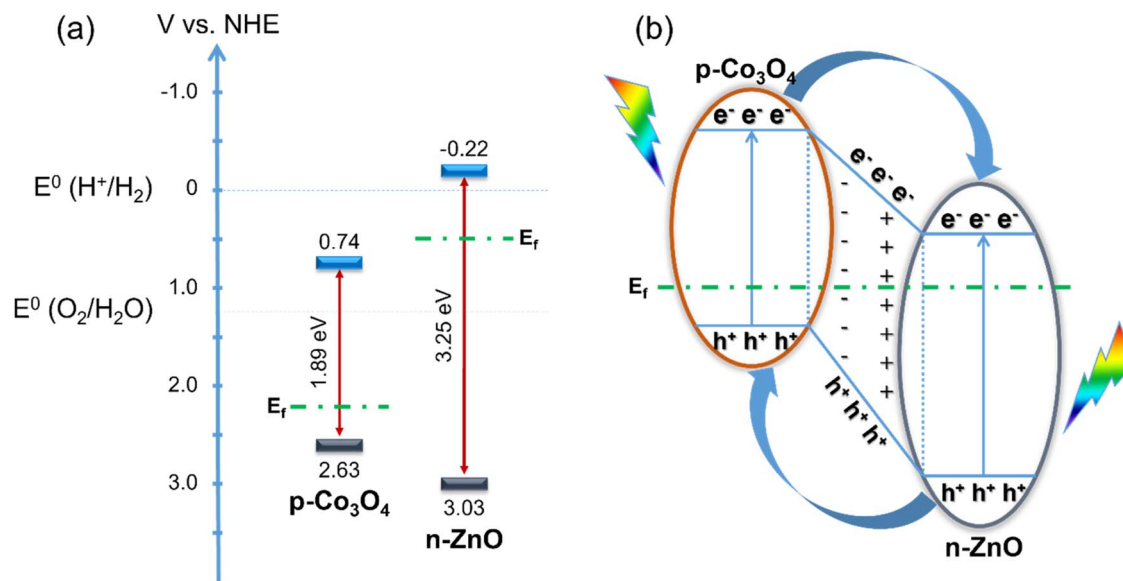**Fig. 8** Energy diagram of ZnO and Co_3O_4 before combination (a) and p–n junction mechanism between ZnO and Co_3O_4 (b).

and electron transfer occurs (Fig. 8b). When they receive sufficient excitation energy, the excited electrons move to the CB while holes are generated on the VB of both Co_3O_4 and ZnO. The electrons on the CB of Co_3O_4 can easily move to the CB of ZnO. At the same time, the holes in the VB of ZnO can also move into the VB of Co_3O_4, all due to the energy difference. It is also known that most of the charge carriers are holes in the p-type semiconductor Co_3O_4 and electrons in the n-type semiconductor ZnO.[48] Due to the concentration gradient, the holes in Co_3O_4 move to ZnO and the electrons in ZnO move to Co_3O_4, leaving oppositely charged ions, thus forming an internal electric field with a direction from ZnO to Co_3O_4. Electrons tend to move opposite to the electric field, leading to the increasing promotion of electrons on the CB of Co_3O_4 to move to the CB of ZnO, helping to increase the electron concentration on ZnO. These electrons directly participate in the water splitting reaction. Therefore, the increasing concentration of electrons in the CB of ZnO increases the photocatalytic activity of the material. In addition, the internal electric field generated at the interface of the two layers of material also plays an important role in slowing down the recombination of the electron–hole pair.[33] This also significantly enhances the photocatalytic activity of the material.

4. Conclusions

The synthesis of the Co_3O_4/ZnO/FTO electrode was achieved using a two-step method. The optimal parameters for electrodeposition of ZnO and Co_3O_4 were 5 min and 2 min, respectively. This approach was found to be cost-effective and timesaving for synthesizing this type of photochemical electrode. The determination of the formation of the p–n junction was also checked by Mott–Schottky plots and some characterization studies. The Co_3O_4-2 and ZnO combination resulted in the formation of p–n junctions, effectively slowing down the

recombination of electron–hole pairs. Furthermore, the Co_3O_4/ZnO heterojunction electrode expressed a high photo-response ability and the photocurrent density of the Co_3O_4-2/ZnO sample is 1.4 times higher than that of the ZnO sample. For the OER, illumination led to overpotentials in the Co_3O_4-2/ZnO samples that were 2.7 times lower than those observed in the ZnO samples. Similarly, for the HER, the illuminated Co_3O_4-2/ZnO sample, an onset potential of −0.5 V and an overpotential of 670 mV were observed, both of which were lower than the onset potential of −0.7 V and overpotential of 900 mV observed in the non-illuminated sample. In the near future, this combination facilitated efficient visible light absorption, making it a favorable choice for developing highly efficient PEC electrodes for overall water splitting.

Conflicts of interest

There are no conflicts to declare.

Acknowledgements

References

1 S. Kundu, K. Bramhaiah and S. Bhattacharyya, Carbon-based nanomaterials: in the quest of alternative metal-free photocatalysts for solar water splitting, *Nanoscale Adv.*, 2020, **2**, 5130–5151.

2 Y.-W. Dong, X.-J. Zhai, Y. Wu, Y.-N. Zhou, Y.-C. Li, J. Nan, S.-T. Wang, Y.-M. Chai and B. Dong, Construction of n-type homogeneous to improve interfacial carrier transfer for enhanced photoelectrocatalytic hydrolysis, *J. Colloid Interface Sci.*, 2024, **658**, 258–266.

3 T. Hisatomi and K. Domen, Reaction systems for solar hydrogen production *via* water splitting with particulate semiconductor photocatalysts, *Nat. Catal.*, 2019, **2**, 387–399.

4 Z. U. Khan, M. Alsaiari, M. A. Ahmed, N. Muhammad, M. Tariq, A. Rahim and A. Niaz, in *Materials for Hydrogen Production, Conversion, and Storage*, John Wiley & Sons, Ltd, 2023, pp. 225–247.

5 R.-Y. Fan, Y.-N. Zhou, M.-X. Li, J.-Y. Xie, W.-L. Yu, J.-Q. Chi, L. Wang, J.-F. Yu, Y.-M. Chai and B. Dong, *In situ* construction of Fe(Co)OOH through ultra-fast electrochemical activation as real catalytic species for enhanced water oxidation, *Chem. Eng. J.*, 2021, **426**, 131943.

6 X. Zhang, C. Feng, B. Dong, C. Liu and Y. Chai, High-Voltage-Enabled Stable Cobalt Species Deposition on MnO_2 for Water Oxidation in Acid, *Adv. Mater.*, 2023, **35**, 2207066.

7 P. Zhou, I. A. Navid, Y. Ma, Y. Xiao, P. Wang, Z. Ye, B. Zhou, K. Sun and Z. Mi, Solar-to-hydrogen efficiency of more than 9% in photocatalytic water splitting, *Nature*, 2023, **613**, 66–70.

8 S. Wang, G. Liu and L. Wang, Crystal Facet Engineering of Photoelectrodes for Photoelectrochemical Water Splitting, *Chem. Rev.*, 2019, **119**, 5192–5247.

9 C. Acar and I. Dincer, A review and evaluation of photoelectrode coating materials and methods for photoelectrochemical hydrogen production, *Int. J. Hydrogen Energy*, 2016, **41**, 7950–7959.

10 C. Murugan and A. Pandikumar, Reinforcement of Visible-Light Harvesting and Charge-Transfer Dynamics of $BiVO_4$ Photoanode *via* Formation of p–n Heterojunction with CuO for Efficient Photoelectrocatalytic Water Splitting, *ACS Appl. Energy Mater.*, 2022, **5**, 6618–6632.

11 C. Murugan, K. B. Bhojanaa, W.-J. Ong, K. Jothivenkatachalam and A. Pandikumar, Improving hole mobility with the heterojunction of graphitic carbon nitride and titanium dioxide *via* soft template process in photoelectrocatalytic water splitting, *Int. J. Hydrogen Energy*, 2019, **44**, 30885–30898.

12 A. R. Fareza, F. A. A. Nugroho, F. F. Abdi and V. Fauzia, Nanoscale metal oxides–2D materials heterostructures for photoelectrochemical water splitting—a review, *J. Mater. Chem. A*, 2022, **10**, 8656–8686.

13 C. Murugan, A. S. Mary, R. Velmurugan, B. Subramanian, P. Murugan and A. Pandikumar, Investigating the interfacial charge transfer between electrodeposited $BiVO_4$ and pulsed laser-deposited Co_3O_4 p–n junction photoanode in photoelectrocatalytic water splitting, *Chem. Eng. J.*, 2024, **483**, 149104.

14 A. S. Mary, C. Murugan and A. Pandikumar, Uplifting the charge carrier separation and migration in Co-doped $CuBi_2O_4/TiO_2$ p–n heterojunction photocathode for enhanced photoelectrocatalytic water splitting, *J. Colloid Interface Sci.*, 2022, **608**, 2482–2492.

15 S. Vinoth and A. Pandikumar, Ni integrated S-gC$_3$N$_4$/BiOBr based Type-II heterojunction as a durable catalyst for photoelectrochemical water splitting, *Renewable Energy*, 2021, **173**, 507–519.

16 J. Yadav and J. P. Singh, WO_3/Ag_2S type-II hierarchical heterojunction for improved charge carrier separation and photoelectrochemical water splitting performance, *J. Alloys Compd.*, 2022, **925**, 166684.

17 Z. Kang, H. Si, S. Zhang, J. Wu, Y. Sun, Q. Liao, Z. Zhang and Y. Zhang, Interface Engineering for Modulation of Charge Carrier Behavior in ZnO Photoelectrochemical Water Splitting, *Adv. Funct. Mater.*, 2019, **29**, 1808032.

18 S. Wang, W. Hao, M. Chen, Y. Han, C. Cheng, L. Shen, G. Ji, A. Song, Z. Zhang and X. Lu, Fabrication of $ZnSn(OH)_6/ZnO/BiOBr$ with high photocatalytic efficiency in removal of various organic pollutants, *J. Alloys Compd.*, 2022, **896**, 162920.

19 U. Pratomo, R. Adhia Pratama, A. Pramudya Sulaeman, Irkham, G. T. M. Kadja, M. Khalil and I. Primadona, Enhancement of the ZnO nanotube photoelectrochemical performance by MXene layer, *Mater. Lett.*, 2023, **337**, 133932.

20 C. M. Taylor, A. Ramirez-Canon, J. Wenk and D. Mattia, Enhancing the photo-corrosion resistance of ZnO nanowire photocatalysts, *J. Hazard. Mater.*, 2019, **378**, 120799.

21 T. L. Simonenko, N. P. Simonenko, P. Yu. Gorobtsov, A. S. Mokrushin, V. R. Solovey, V. M. Pozharnitskaya, E. P. Simonenko, O. V. Glumov, N. A. Melnikova, A. A. Lizunova, M. G. Kozodaev, A. M. Markeev, I. A. Volkov, V. G. Sevastyanov and N. T. Kuznetsov, Pen plotter printing of Co_3O_4 thin films: features of the microstructure, optical, electrophysical and gas-sensing properties, *J. Alloys Compd.*, 2020, **832**, 154957.

22 A. UmaSudharshini, M. Bououdina, M. Venkateshwarlu, C. Manoharan and P. Dhamodharan, Low temperature solvothermal synthesis of pristine Co_3O_4 nanoparticles as potential supercapacitor, *Surf. Interfaces*, 2020, **19**, 100535.

23 M. Etzi Coller Pascuzzi, M. van Velzen, J. P. Hofmann and E. J. M. Hensen, On the Stability of Co_3O_4 Oxygen Evolution Electrocatalysts in Acid, *ChemCatChem*, 2021, **13**, 459–467.

24 A. L. Bhatti, A. Tahira, A. Gradone, R. Mazzaro, V. Morandi, U. aftab, M. I. Abro, A. Nafady, K. Qi, A. Infantes-Molina, A. Vomiero and Z. H. Ibupoto, Nanostructured Co_3O_4 electrocatalyst for OER: The role of organic polyelectrolytes as soft templates, *Electrochim. Acta*, 2021, **398**, 139338.

25 C. Daulbayev, F. Sultanov, B. Bakbolat and O. Daulbayev, 0D, 1D and 2D nanomaterials for visible photoelectrochemical water splitting. A Review, *Int. J. Hydrogen Energy*, 2020, **45**, 33325–33342.

26 G. Mohamed Reda, H. Fan and H. Tian, Room-temperature solid state synthesis of Co_3O_4/ZnO p–n heterostructure and its photocatalytic activity, *Adv. Powder Technol.*, 2017, **28**, 953–963.

27 M. Li, S. Zhang, L. Li, J. Han, X. Zhu, Q. Ge and H. Wang, Construction of Highly Active and Selective Polydopamine Modified Hollow ZnO/Co_3O_4 p–n Heterojunction Catalyst for Photocatalytic CO_2 Reduction, *ACS Sustainable Chem. Eng.*, 2020, **8**, 11465–11476.

28 V. Anh Tran, T. Khoa Phung, V. Thuan Le, T. Ky Vo, T. Tai Nguyen, T. Anh Nga Nguyen, D. Quoc Viet, V. Quang Hieu and T.-T. Thi Vo, Solar-light-driven photocatalytic

degradation of methyl orange dye over Co_3O_4-ZnO nanoparticles, *Mater. Lett.*, 2021, **284**, 128902.

29 N. Koteeswara Reddy, S. Winkler, N. Koch and N. Pinna, Electrochemical Water Oxidation of Ultrathin Cobalt Oxide-Based Catalyst Supported onto Aligned ZnO Nanorods, *ACS Appl. Mater. Interfaces*, 2016, **8**, 3226–3232.

30 S.-K. Min, H. Kim, Y. Noh, K.-S. Choi and S.-P. Chang, Fabrication of highly sensitive and selective acetone sensor using (p)-Co_3O_4 nanoparticle-decorated (n)-ZnO nanowires, *Thin Solid Films*, 2020, **714**, 138249.

31 H. Wang, H. Wang, L. Li, Y. Gu, B.-H. Kim and J. Huang, Self-Powered Broadband Photodetectors Material Based on Co_3O_4–ZnO Heterojunction with Bottlebrush Nanostructure, *ACS Appl. Electron. Mater.*, 2023, **5**, 3224–3231.

32 A. A. Markhabayeva, Z. K. Kalkozova, R. Nemkayeva, Y. Yerlanuly, A. S. Anarova, M. A. Tulegenova, A. T. Tulegenova and K. A. Abdullin, Construction of a ZnO Heterogeneous Structure Using Co_3O_4 as a Co-Catalyst to Enhance Photoelectrochemical Performance, *Materials*, 2024, **17**, 146.

33 Y. Yang, W. Cheng and Y. F. Cheng, Preparation of Co_3O_4@ZnO core-shell nanocomposites with intrinsic p–n junction as high-performance photoelectrodes for photoelectrochemical cathodic protection under visible light, *Appl. Surf. Sci.*, 2019, **476**, 815–821.

34 F. Ahmed, S. Kumar, N. Arshi, M. S. Anwar, L. Su-Yeon, G.-S. Kil, D.-W. Park, B. H. Koo and C. G. Lee, Preparation and characterizations of polyaniline (PANI)/ZnO nanocomposites film using solution casting method, *Thin Solid Films*, 2011, **519**, 8375–8378.

35 A. Mahajan, P. Deshpande and S. Butee, Synthesis and characterization of NiO/ZnO composite prepared by solid-state reaction method, *Mater. Today: Proc.*, 2022, **50**, 1912–1917.

36 S. Kandula and P. Jeevanandam, A facile synthetic approach for SiO_2@Co_3O_4 core–shell nanorattles with enhanced peroxidase-like activity, *RSC Adv.*, 2014, **5**, 5295–5306.

37 Y. Sun, C. Wang, S. Qin, F. Pan, Y. Li, Z. Wang and C. Qin, Co_3O_4 Nanopetals Grown on the Porous CuO Network for the Photocatalytic Degradation, *Nanomaterials*, 2022, **12**, 2850.

38 R. Bhargava, S. Khan, N. Ahmad and M. M. Ansari, Investigation of structural, optical and electrical properties of Co3O4 nanoparticles, *AIP Conf. Proc.*, 2018, **1953**, 030034.

39 L. Saikia, D. Bhuyan, M. Saikia, B. Malakar, D. K. Dutta and P. Sengupta, Photocatalytic performance of ZnO nanomaterials for self sensitized degradation of malachite green dye under solar light, *Appl. Catal., A*, 2015, **490**, 42–49.

40 J. Wang, Y. Shen, X. Li, Y. Xia and C. Yang, Synergistic effects of UV activation and surface oxygen vacancies on the room-temperature NO_2 gas sensing performance of ZnO nanowires, *Sens. Actuators, B*, 2019, **298**, 126858.

41 J. H. Baek, B. J. Kim, G. S. Han, S. W. Hwang, D. R. Kim, I. S. Cho and H. S. Jung, $BiVO_4$/WO_3/SnO_2 Double-Heterojunction Photoanode with Enhanced Charge Separation and Visible-Transparency for Bias-Free Solar Water-Splitting with a Perovskite Solar Cell, *ACS Appl. Mater. Interfaces*, 2017, **9**, 1479–1487.

42 Y. Li, J. Feng, H. Li, X. Wei, R. Wang and A. Zhou, Photoelectrochemical splitting of natural seawater with α-Fe_2O_3/WO_3 nanorod arrays, *Int. J. Hydrogen Energy*, 2016, **41**, 4096–4105.

43 Q. Liu, F. Cao, F. Wu, W. Tian and L. Li, Interface reacted $ZnFe_2O_4$ on α-Fe_2O_3 nanoarrays for largely improved photoelectrochemical activity, *RSC Adv.*, 2015, **5**, 79440–79446.

44 C.-H. Wang, D.-D. Qin, D.-L. Shan, J. Gu, Y. Yan, J. Chen, Q.-H. Wang, C.-H. He, Y. Li, J.-J. Quan and X.-Q. Lu, Assembly of g-C_3N_4-based type II and Z-scheme heterojunction anodes with improved charge separation for photoelectrojunction water oxidation, *Phys. Chem. Chem. Phys.*, 2017, **19**, 4507–4515.

45 S. Majumder, N. D. Quang, N. M. Hung, N. D. Chinh, C. Kim and D. Kim, Deposition of zinc cobaltite nanoparticles onto bismuth vanadate for enhanced photoelectrochemical water splitting, *J. Colloid Interface Sci.*, 2021, **599**, 453–466.

46 S. Wang, W. Hao, M. Chen, Y. Han, C. Cheng, L. Shen, G. Ji, A. Song, Z. Zhang and X. Lu, Fabrication of $ZnSn(OH)_6$/ZnO/BiOBr with high photocatalytic efficiency in removal of various organic pollutants, *J. Alloys Compd.*, 2022, **896**, 162920.

47 M. Abdelfatah, N. Darwesh, H. Atta, A. M. Beltagi, B. Sun, A. El-Shaer and W. Ismail, Inverting electrodeposited nanostructured Cu_2O thin films from n-type to p-type semiconductors and variation of their physical and photoelectrochemical properties for optoelectronic applications, *Ceram. Int.*, 2023, **49**, 30732–30743.

48 L. Zhang, H. Li, B. Yang, Y. Zhou, Z. Zhang and Y. Wang, Photo-deposition of ZnO/Co_3O_4 core-shell nanorods with p–n junction for efficient oxygen evolution reaction, *J. Solid State Electrochem.*, 2019, **23**, 3287–3297.